

SRGS: Super-Resolution 3D Gaussian Splatting

Xiang Feng*, Yongbo He*, Yubo Wang, Yan Yang, Wen Li, Yifei Chen, Zhenzhong Kuang, Jiajun Ding†, Jianping Fan, *Senior member, IEEE*, Jun Yu, *Senior member, IEEE*

Abstract—Recently, 3D Gaussian Splatting (3DGS) has gained popularity as a novel explicit 3D representation. This approach relies on the representation power of Gaussian primitives to provide a high-quality rendering. However, primitives optimized at low resolution inevitably exhibit sparsity and texture deficiency, posing a challenge for achieving high-resolution novel view synthesis (HRNVS). To address this problem, we propose Super-Resolution 3D Gaussian Splatting (SRGS) to perform the optimization in a high-resolution (HR) space. The sub-pixel constraint is introduced for the increased sampling points in HR space, exploiting the sub-pixel cross-view information of the multiple low-resolution (LR) views. The gradient accumulated from more sampling points will facilitate the densification of primitives. Furthermore, a pre-trained 2D super-resolution model is integrated with the sub-pixel constraint, enabling these dense primitives to learn faithful texture features. In general, our method focuses on densification and texture learning to effectively enhance the representation ability of primitives. Experimentally, our method achieves high rendering quality on HRNVS only with LR inputs, outperforming state-of-the-art methods on challenging datasets such as Mip-NeRF 360 and Tanks & Temples. The code will be available at the following link: <https://github.com/XiangFeng66/SR-GS>.

Index Terms—3D Gaussian Splatting, Super Resolution, Novel View Synthesis.

I. INTRODUCTION

Novel View Synthesis (NVS) is a long-standing challenge in computer vision and graphics. The advancements in Neural Radiance Field (NeRF) [1] have demonstrated the potential of implicit neural representation on NVS. Most recently, 3D Gaussian Splatting (3DGS) [2] has gained popularity with a primitive-based representation, outperforming NeRF in terms of both rendering speed and reconstruction quality. While 3DGS has several advantages against previous methods, it suffers from sharply degraded renderings when performing high-resolution novel view synthesis (HRNVS) [3] with only LR inputs.

In 3DGS, the representation power of Gaussian primitives is vital to achieving high-quality view synthesis. Specifically,

*Equal contribution, †Corresponding author.

Xiang Feng, Yongbo He, Yubo Wang, Yan Yang, Zhenzhong Kuang, Jun Yu, Jianping Fan, Jiajun Ding are with School of Computer Science and Technology, Hangzhou Dianzi University, Hangzhou, China, 310018. Email: xiangfeng@hdu.edu.cn, rsth@hdu.edu.cn, yangyan@hdu.edu.cn, zzkuang@hdu.edu.cn, yujun@hdu.edu.cn, dj@hdu.edu.cn.

Jianping Fan is with AI Lab at Lenovo Research, Beijing, China. Email: jfan1@lenovo.com.

Wen Li is with School of Computer Science and Technology, Jiangxi Normal University, Jiangxi, China, 330022. Email: wenl0110@163.com

Yifei Chen is with HDU-ITMO Joint Institute, Hangzhou Dianzi University, Hangzhou, 310018, China. Email: cheniyifei@hdu.edu.cn

This work is supported by the Natural Science Foundation of China (Grant No. 62206082), Zhejiang Provincial Natural Science Foundation of China (Grant No. LY22F020028, No. LQ21F020014, No. LQ24F020032), and the National College Student Innovation and Entrepreneurship Program Project (Grant No. 202310336001).

faithful rendering at high resolution requires denser Gaussian primitives with fine-grained texture features [4]. However, there are two limitations for primitives to synthesize views at a higher resolution: (1) **Sparsity**: Due to the adaptive control strategy proposed by 3DGS, coarse information is rendered with sparse primitives. Thus, the primitives optimized for low-resolution (LR) scenes are inevitably sparsely distributed in space, leading to the artifacts in the rendered HR views. (2) **Texture Deficiency**: Existing LR views lack the essential HR textures. Therefore, it is impossible for the primitives in 3D space to learn the corresponding features without the back-projection of HR textures. To address these limitations, we propose Super-Resolution 3D Gaussian Splatting (SRGS), which extends 3DGS to achieve high-quality HRNVS. The proposed method comprises two parts, i.e., Super-Resolution Gaussian Densification and Texture-Guided Gaussian Learning.

Super-Resolution Gaussian Densification. According to the strategy of adaptive density control, low-frequency areas are represented by sparse and large primitives, whereas high-frequency areas are represented by dense and small primitives. However, the Gaussian field reconstructed from existing LR views inevitably results in fewer and larger primitives, posing challenges in rendering HR views that contain high-frequency information. Therefore, our key insight is that Gaussian densification is essential in enhancing the representation power of primitives for HR rendering. To promote densification, radiance field optimization is performed in HR space using the super-splatting method. Afterwards, a sub-pixel constraint is employed to exploit the cross-view information from the increased sampling points. The gradient accumulated from more sampling points will encourage the adaptive cloning or splitting of Gaussian primitives, resulting in a denser and more accurate Gaussian field.

Texture-Guided Gaussian Learning. As an inverse rendering method, the features of Gaussian primitives are learned through the back-projection process from 2D views. However, existing LR views suffer from the lack of HR textures, making it challenging for the primitives to capture detailed features only from LR views. Despite optimizing the primitives in the HR space, incorrect textures may still appear in the rendered images. Thus, a pre-trained 2D SR model is introduced, serving as the external prior and providing HR reference views with rich textures. Due to the lack of 3D awareness, the 2D SR model inevitably produces inconsistent textures when processing multiple views, leading to spatial ambiguity in 3D space. In our method, the sub-pixel constraint is performed via existing views with realistic textures, which serves as a regularizer to alleviate the presence of incorrect texture features. In this way, Gaussian primitives tend to learn the faithful texture feature while avoiding spatial ambiguity.

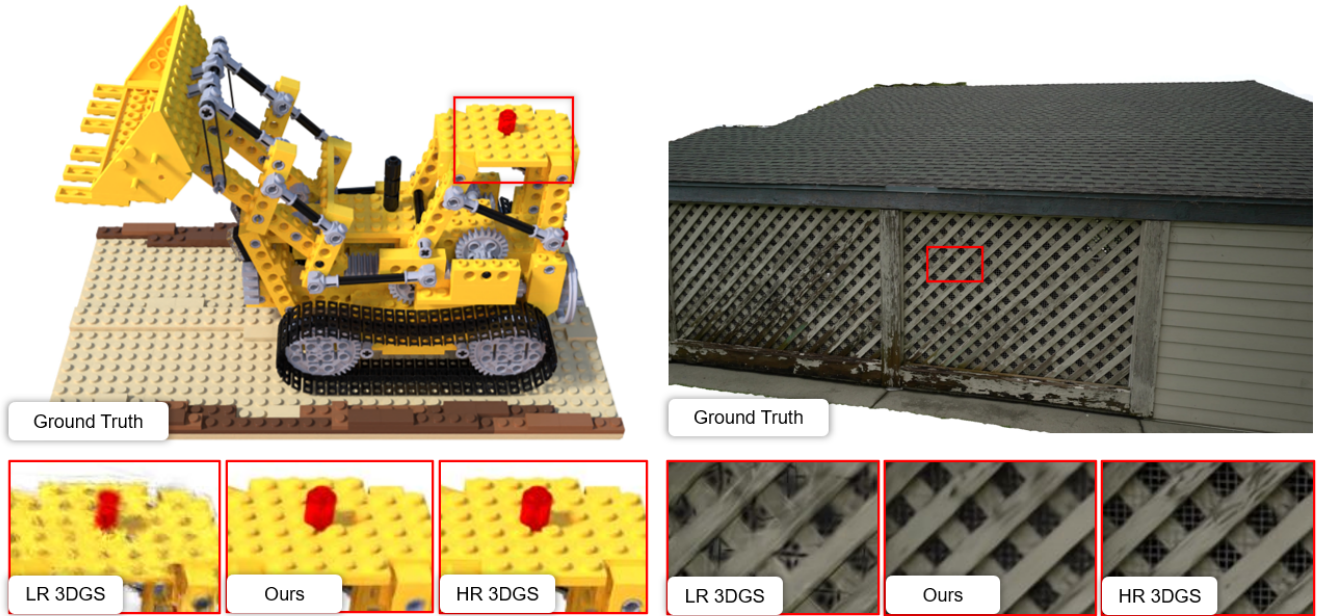


Fig. 1: Our method significantly enhances the representation power of Gaussian primitives, achieving a rendering quality close to HR-3DGS.

Through densification and texture learning, SRGS effectively achieves faithful rendering at high resolution with detailed textures. The qualitative evaluation of the Lego is demonstrated in Fig. 1. It can be obviously observed that SRGS significantly improves the rendering results reconstructed from LR views, with performance approaching that of HR 3DGS. This also validates that SRGS effectively enhances the representation power of Gaussian primitives. Moreover, comprehensive experiments show that the rendering quality of SRGS outperforms existing state-of-the-art methods.

In summary, our contributions are as follows:

- To the best of our knowledge, we are the first to focus on the HRNVS of 3DGS. Our method achieves high-quality HRNVS only with existing LR views.
- We propose leveraging a Super-Resolution Gaussian Densification strategy, effectively facilitating the generation of denser and more accurate Gaussian primitives.
- We introduce a Texture-Guided Gaussian Learning strategy that guides Gaussian primitives to learn faithful texture from the external priors of 2D SR model.
- Experiments on various challenging datasets show that the proposed method significantly outperforms existing methods in terms of rendering quality for HRNVS.

II. RELATED WORKS

A. Novel View Synthesis

Novel View Synthesis (NVS) is a challenging task that synthesizes a target image with an arbitrary target camera pose from the given source images and their camera poses [5], [6]. Neural Radiance Field (NeRF) [1] combines implicit scene representation with volume rendering [7]–[10], demonstrating impressive view synthesis performance. However, dense point sampling remains challenging in terms of rendering speed.

Methods for NeRF acceleration mostly focus on replacing vanilla MLPs [11]–[13] with different variants of space discretization, such as voxel grids [14]–[18], hash encoding [19]–[21], tensor radiation fields [22]–[26], etc. Furthermore, some methods [27]–[31] distill a pretrained NeRF into a sparse representation, enabling real-time rendering of NeRFs. Recently, the advancements in 3D Gaussian Splatting (3DGS) [2] prove that continuous representation is not strictly necessary. 3DGS represents the 3D scene as a set of parameterized 3D Gaussian primitives, achieving real-time rendering with fast splat-based rasterization. However, primitives optimized for LR space tend to exhibit sparsity and texture deficiency, making it difficult for 3DGS to achieve high-quality high-resolution rendering. In this regard, Mip-Splatting introduces a 3D smoothing filter to eliminate artifacts, but it struggles to generate the texture details required for HRNVS with only LR inputs.

B. Image Super-Resolution

Image super-resolution aims to learn the inverse function of image degradation. It has made significant advancements with the rise of deep learning techniques driven by large-scale datasets [32]–[35]. For example, EDSR [36] and RCAN [37] achieve image super-resolution with deep network structures using residual blocks and the attention mechanism, respectively. Then, with the advent of the transformer, SwinIR [38] used the Swin-Transformer, proving the efficacy of long-distance dependency modeling on image super-resolution. In addition, some methods use discriminative networks [39]–[43] and diffusion models [44]–[47] to improve the perceptual quality of image super-resolution. The well-trained super-resolution models can recover complex textures from low resolutions. However, Single-Image Super-Resolution (SISR) models inevitably produce inconsistent textures when per-

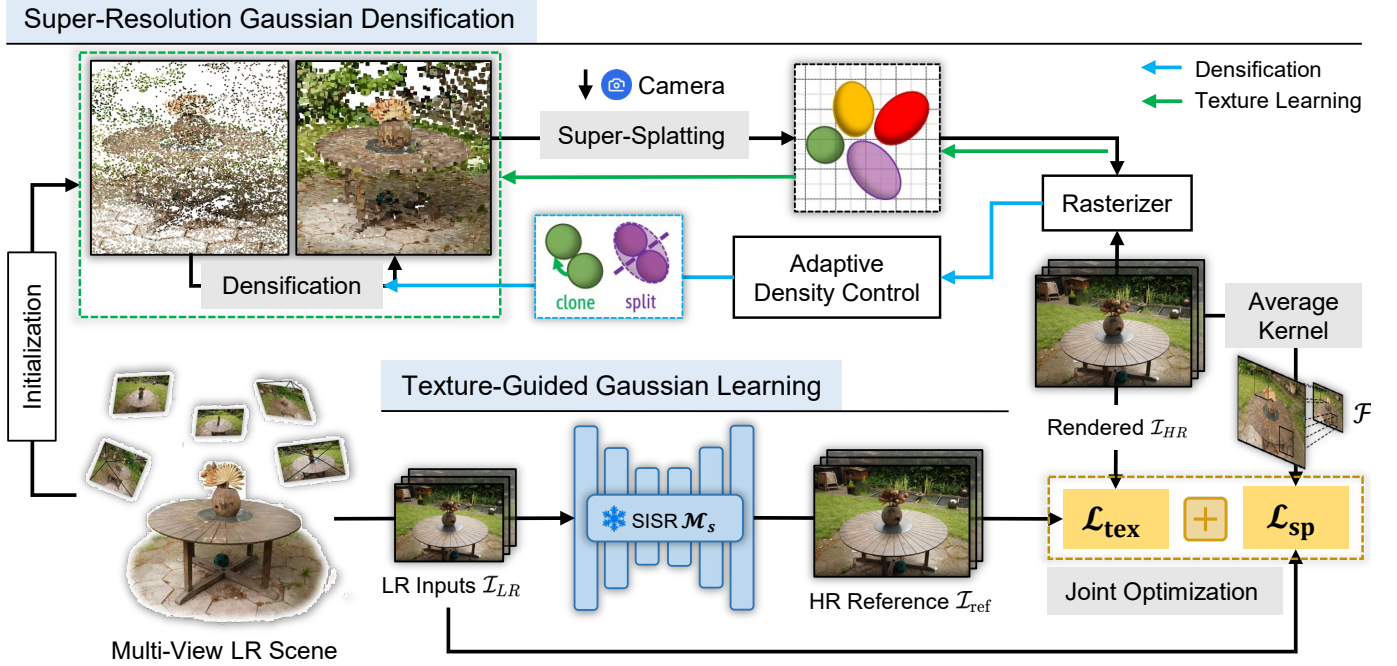


Fig. 2: Overview of the proposed method. SRGS is composed of Super-Resolution Gaussian Densification (SRGD) and Texture-Guided Gaussian Learning (TGGL). In SRGD, the radiance field optimization is performed in the HR space through the super-splatting method. The sub-pixel constraint \mathcal{L}_{sp} supervises the increased sampling points in the HR space. The gradient from more sampling points promotes Gaussian densification through cloning and splitting. In TGGL, a 2D SR model \mathcal{M}_s is utilized to generate HR reference views \mathcal{I}_{ref} , providing detailed textures absent from \mathcal{I}_{LR} . With the joint optimization of \mathcal{I}_{sp} and \mathcal{I}_{tex} , the Gaussian primitives tend to learn faithful texture features from the external priors.

formed separately on multi-view images. Although 3DGS can force 3D consistency, inconsistent textures will lead to spatial ambiguity. In this study, we introduce external texture knowledge into Gaussian primitives to enhance texture richness. Meanwhile, we propose leveraging the sub-pixel constraint from existing LR views to mitigate the incorrect textures caused by SISR models.

C. Super-Resolution Radiance Fields

It remains challenging for radiance field methods to achieve HRNVS only with LR multi-view scenes. Recent works have mostly focused on NeRF [1] and its variants. The pioneering work is NeRF-SR [48], which exploits the 3D consistency of NeRF, improving rendering quality through a super-sampling strategy and depth-guided refinement. The current state-of-the-art model, CROC [3], proposes a novel framework for performing cross-guided radiance field optimization using the Single Image Super-Resolution (SISR) model. Moreover, multiscale-aware methods such as Mip-NeRF [49] and its variants (e.g., Zip-NeRF [50] and Mip-NeRF 360 [51]) achieve high performance when changing the rendering resolution. To the best of our knowledge, our method is the first to enhance the performance of HRNVS based on the 3DGS [2] only with LR inputs. In the method, a densification strategy is presented to facilitate the generation of denser and more accurate Gaussian primitives, allowing for 3DGS to represent intricate high-resolution features. Meanwhile, Gaussian primitives learn

faithful texture features with both the external knowledge from the SISR model and the constraints of existing LR views. It is worth noting that our method does not require other scene data training compared with CROC.

III. PRELIMINARIES

Scene representation. Given a training dataset \mathcal{I} composed of multi-view 2D images with camera poses, 3DGS learns a set of 3D colored Gaussian primitives $\mathcal{G} = \{\mathbf{g}_1, \mathbf{g}_2, \dots, \mathbf{g}_N\}$, where N denotes the number of 3D Gaussian primitives in the scene. For any Gaussian primitive $\mathbf{g} \in \mathcal{G}$, 3DGS models it as a \mathbf{g}^{3D} with the mean vector $\boldsymbol{\mu}$ and covariance matrix $\boldsymbol{\Sigma}$:

$$\mathbf{g}^{3D}(\mathbf{x}|\boldsymbol{\mu}, \boldsymbol{\Sigma}) = \exp\left(-\frac{1}{2}(\mathbf{x} - \boldsymbol{\mu})^\top \boldsymbol{\Sigma}^{-1}(\mathbf{x} - \boldsymbol{\mu})\right) \quad (1)$$

where $\boldsymbol{\mu} \in \mathbb{R}^3$ is the position of primitive \mathbf{g} , and $\boldsymbol{\Sigma} \in \mathbb{R}^{3 \times 3}$ is an anisotropic covariance matrix, which is factorized into a scaling matrix \mathbf{S} and a rotation matrix \mathbf{R} as $\boldsymbol{\Sigma} = \mathbf{R}\mathbf{S}\mathbf{S}^\top \mathbf{R}^\top$.

Rasterization rendering. Given a specific camera pose, extrinsic matrix \mathbf{T} and projection matrix \mathbf{K} , 3DGS projects the 3D Gaussian primitive to 2D. The projected position $\hat{\boldsymbol{\mu}}$ and covariance matrix $\hat{\boldsymbol{\Sigma}}$ in 2D screen space are denoted as:

$$\hat{\boldsymbol{\mu}} = \mathbf{K}\mathbf{T}[\boldsymbol{\mu}, 1]^\top, \quad \hat{\boldsymbol{\Sigma}} = \mathbf{J}\mathbf{T}\boldsymbol{\Sigma}\mathbf{T}^\top \mathbf{J}^\top, \quad (2)$$

where \mathbf{J} is the Jacobian matrix of the affine approximation of the perspective projection. The projected 2D Gaussian signal

for the pixel u is given:

$$g^{2D}(u|\hat{\mu}, \hat{\Sigma}) = \exp\left(-\frac{1}{2}(u - \hat{\mu})^\top \hat{\Sigma}^{-1}(u - \hat{\mu})\right). \quad (3)$$

With the projected 2D Gaussian signal, 3DGS derives the volume transmittance and shades the color of pixel u through:

$$C(u) = \sum_{i \in N} T_i g_i^{2D}(u|\hat{\mu}_i, \hat{\Sigma}_i) \alpha_i c_i, \quad (4)$$

$$T_i = \prod_{j=1}^{i-1} (1 - g_j^{2D}(u|\hat{\mu}_j, \hat{\Sigma}_j) \alpha_j) \quad (5)$$

where c_i is the color of each Gaussian primitive and α_i is given by evaluating a 2D Gaussian with covariance $\hat{\Sigma}$ multiplied with a learned per-primitive opacity.

Optimization. To reconstruct a scene, given a set of multi-view input images with known camera poses, the 3DGS per scene is optimized by minimizing the following loss:

$$\mathcal{L}_{gs} = (1 - \lambda)\mathcal{L}_1 + \lambda\mathcal{L}_{D-SSIM} \quad (6)$$

where $\lambda = 0.2$ is used in all tests.

Moreover, a gradient-based controller is presented to adaptively manage the density of 3D Gaussian. For Gaussian i under viewpoint k , the NDC coordinate is $(\mu_{ndc,x}^{i,k}, \mu_{ndc,y}^{i,k}, \mu_{ndc,z}^{i,k})$, and the loss under viewpoint k is L_k . Gaussian i participates in the calculation for M^i viewpoints in every 3000 iterations. When Gaussian satisfies

$$\nabla g = \frac{\sum_{k=1}^{M^i} \sqrt{\left(\frac{\partial L_k}{\partial \mu_{ndc,x}^{i,k}}\right)^2 + \left(\frac{\partial L_k}{\partial \mu_{ndc,y}^{i,k}}\right)^2}}{M^i} > \tau_{pos}, \quad (7)$$

it is transformed into two Gaussians. τ_{pos} refers to the threshold for cloning or splitting [52].

IV. APPROACH

3DGS exhibits sharply degraded renderings when synthesizing HR views. This is mainly because primitives struggle to gain the capability from LR views to represent HR information. To this end, our method performs the optimization in a HR space, enhancing the representation power of Gaussian primitives through densification (Sec.IV-A) and texture learning (Sec.IV-B). Consequently, 3DGS can produce novel views that approach HR ground truth.

A. Super-Resolution Gaussian Densification

In 3DGS models, the adaptive Gaussian densification scheme is utilized to control the number of Gaussians and their density over a unit volume. In this scheme, the density of primitives mostly depends on the richness of geometric features. However, the LR views contain fewer details compared to the HR views. Therefore, the optimization using LR views mostly yields sparser Gaussian primitives. These sparse primitives struggle to reconstruct the fine-grained details present in the HR views. As illustrated in Fig. 3, a single primitive in LR space occupies a larger pixel area when upscaled to HR space, leading to blurry artifacts in rendered views. In this section, a super-resolution Gaussian densification method is



Fig. 3: Even if a large primitive is well trained in LR space, it tends to cause blurring artifacts when upscaled to HR space. To preserve fine-grained details at high resolutions, it is crucial to use more primitives during the reconstruction process.

introduced to generate denser primitives in HR space for better representation of the scene. This method comprises super-splating and sub-pixel constraints.

Super-splating. To perform optimization for HR space, a super-splating method is employed to enhance the sampling rate. Specifically, the 2D Gaussian projections in screen space $\{\mathcal{G}_k^{2D} \mid k = 1, \dots, K\}$ are super-resolved to synthesize HR novel views \mathcal{I}_{HR} . This method increases the number of sampling points for each Gaussian primitive, propagating the gradients into the HR 3D space. Referring to Eq. 7, the average gradient of more sampling points is accumulated for the Gaussian primitives.

Sub-pixel constraints. Due to the lack of HR ground truth for supervision, we form the sub-pixel constraint only with LR existing views \mathcal{I}_{LR} . The rendered HR views \mathcal{I}_{HR} are downsampled with an average kernel to align with the existing LR views \mathcal{I}_{LR} :

$$\mathcal{F}^p = \frac{1}{s^2} \sum_{r \in \mathcal{R}_s(p)} \mathcal{I}_{HR}^r \quad (8)$$

where s refers to the super-resolution factor and \mathcal{R}_s is the set of sub-pixels. Therefore, the sub-pixel constraint means that s^2 rays in HR space are constrained by a single pixel in \mathcal{I}_{LR} . The loss function \mathcal{L}_{sp} employs a similar form as Eq. 6, which can be expressed as follows:

$$\mathcal{L}_1^{sp} = \frac{1}{|\mathcal{P}|} \sum_{p \in \mathcal{P}} \|\mathcal{F}^p - \mathcal{I}_{LR}^p\| \quad (9)$$

where \mathcal{P} denotes all pixels of the existing view, and $|\mathcal{P}|$ is the number of pixels in \mathcal{P} .

$$\mathcal{L}_{D-SSIM}^{sp} = 1 - \text{SSIM}(\mathcal{F}, \mathcal{I}_{LR}) \quad (10)$$

$$\mathcal{L}_{sp} = (1 - \lambda)\mathcal{L}_1^{sp} + \lambda\mathcal{L}_{D-SSIM}^{sp} \quad (11)$$

According to the densification condition referenced in Eq. 7, the areas that have large view-space positional gradients are good candidates. In our method, the internal information of LR views is exploited to constrain the increased sampling points. The cross-view information at the sub-pixel level provides a larger positional gradient ∇g in the high-frequency region, encouraging the primitives to adaptively clone or split. Through local densification in the HR space, the 3DGS model can leverage denser and more accurate Gaussian primitives to encode high-resolution texture information.

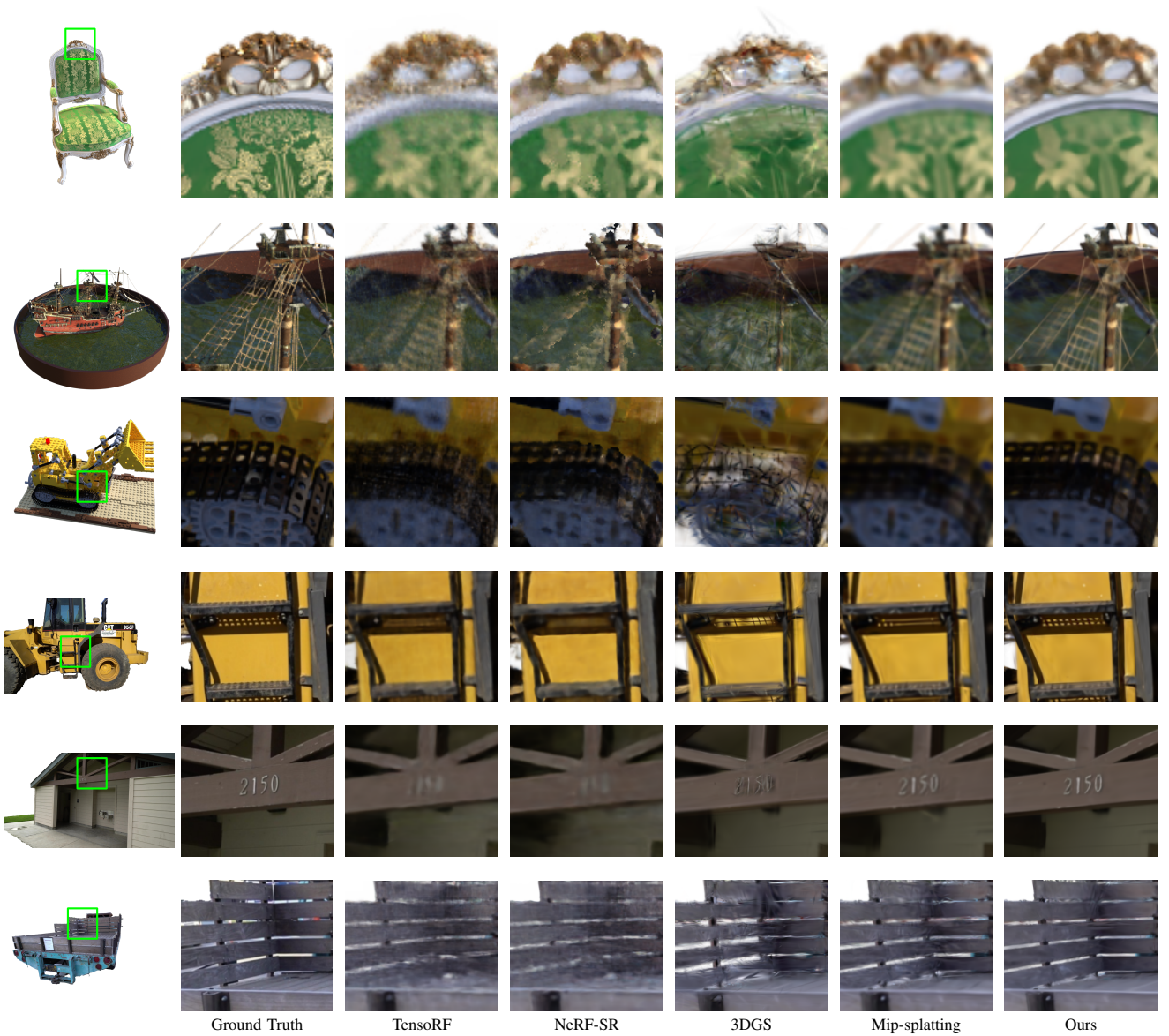


Fig. 4: Qualitative comparison of the HRNVS ($\times 4$) on the Synthetic NeRF and Tanks & Temples datasets. The results are the zoom-in version of the green box region. SRGS (Ours) shows clearer details than TensorRF, NeRF-SR, 3DGS, and Mip-Splatting.

B. Texture-Guided Gaussian Learning

The optimization at the sub-pixel level leverages the internal information of existing LR multiple views, achieving the densification of primitives in HR space. However, owing to the absence of HR textures in the existing LR views, even with dense primitives, it remains challenging to capture high-frequency textures effectively. Therefore, the rendered HR views are still far from the ground truth.

As an inverse rendering method, the features of Gaussian primitives are learned through the back-projection process from 2D views. Hence, a viable approach is to generate the HR textures in 2D and back-project them into 3D. Here, a texture-guided method is proposed to facilitate Gaussian learning using the texture richness of an external model. With extensive prior knowledge derived from large-scale datasets, the 2D SR

model is capable of recovering HR textures from LR views. Specifically, a pretrained 2D SR model \mathcal{M}_s is utilized to generate HR reference views: $\mathcal{I}_{ref} = \mathcal{M}_s(\mathcal{I}_{LR})$. The texture difference between reference views \mathcal{I}_{ref} and rendered views \mathcal{I}_{HR} can guide primitives to encode detailed texture features. The texture learning is supervised by the L1 rendering loss with a D-SSIM term as the same as Eq. 6:

$$\mathcal{L}_{tex} = (1 - \lambda)\mathcal{L}_1(\mathcal{I}_{ref}, \mathcal{I}_{HR}) + \lambda\mathcal{L}_{D-SSIM}(\mathcal{I}_{ref}, \mathcal{I}_{HR}) \quad (12)$$

Previous works [53]–[55] have attempted to integrate 2D and 3D models for the 3D vision tasks but were hindered by the lack of 3D consistency inherent in 2D models. It can be observed that the learning process is misled by inconsistent texture across multiple generated views, causing significant ambiguity in 3D space. This problem is well addressed in our

TABLE I: Quantitative metrics for HRNVS ($\times 2$ and $\times 4$) on Synthetic NeRF and Tanks & Temples datasets: Synthetic $\times 2$ ($400 \times 400 \rightarrow 800 \times 800$), Synthetic $\times 4$ ($200 \times 200 \rightarrow 800 \times 800$), Tanks & Temples $\times 2$ ($960 \times 540 \rightarrow 1920 \times 1080$), Tanks & Temples $\times 4$ ($480 \times 270 \rightarrow 1920 \times 1080$). The performance of HR-3DGS serves as the theoretical upper limit of the HRNVS task.

Method	Synthetic NeRF $\times 2$			Synthetic NeRF $\times 4$			Tanks & Temples $\times 2$			Tanks & Temples $\times 4$		
	PSNR \uparrow	SSIM \uparrow	LPIPS \downarrow	PSNR \uparrow	SSIM \uparrow	LPIPS \downarrow	PSNR \uparrow	SSIM \uparrow	LPIPS \downarrow	PSNR \uparrow	SSIM \uparrow	LPIPS \downarrow
TenSoRF [22]	31.45	0.952	0.049	28.01	0.910	0.113	27.14	0.907	0.148	26.82	0.896	0.174
NeRF-SR [48]	30.08	0.939	0.050	28.90	0.927	0.099	26.78	0.897	0.152	26.36	0.887	0.182
CROC [3]	—	—	—	30.71	0.945	0.067	—	—	—	—	—	—
3DGS [2]	24.64	0.923	0.064	20.31	0.852	0.121	25.84	0.937	0.093	24.02	0.905	0.125
Mip-splatting [56]	31.37	0.957	0.048	28.44	0.930	0.087	27.31	0.947	0.085	26.40	0.929	0.108
SRGS (Ours)	32.67	0.965	0.036	30.83	0.948	0.056	28.44	0.950	0.085	28.18	0.938	0.102
HR-3DGS	33.32	0.974	0.023	33.32	0.974	0.023	28.90	0.953	0.082	28.90	0.953	0.082

TABLE II: Quantitative metrics for HRNVS ($\times 4$ and $\times 8$) on Mip-NeRF 360 dataset, SRGS achieves the best results.

Method	Mip-NeRF 360 $\times 4$			Mip-NeRF 360 $\times 8$		
	PSNR \uparrow	SSIM \uparrow	LPIPS \downarrow	PSNR \uparrow	SSIM \uparrow	LPIPS \downarrow
Mip-NeRF 360 [51]	24.16	0.670	0.370	24.10	0.706	0.428
Zip-NeRF [50]	20.87	0.565	0.421	20.27	0.559	0.494
3DGS [2]	20.71	0.619	0.394	19.59	0.619	0.476
Mip-splatting [56]	26.43	0.754	0.305	26.22	0.765	0.392
SRGS (Ours)	26.88	0.767	0.286	26.57	0.775	0.377

method. The Gaussian learning is affected by the gradient of two parts: the texture loss \mathcal{L}_{tex} and the sub-pixel loss \mathcal{L}_{sp} . The total loss function \mathcal{L} is defined as:

$$\mathcal{L} = (1 - \lambda_e)\mathcal{L}_{sp} + \lambda_e\mathcal{L}_{tex} \quad (13)$$

where λ_e is set to 0.4 in training and the analysis of this parameter is shown in the Sec.V-F.

Since the sub-pixel constraint comes from realistic views with faithful texture, Gaussian primitives tend to encode texture features that match the ground truth. The incorrect textures introduced from the external model will cause a rise in sub-pixel loss \mathcal{L}_{sp} , forming a regularization effect for external texture learning. Overall, the joint optimization mechanism involving both \mathcal{L}_{tex} and \mathcal{L}_{sp} facilitates the generation of intricate and faithful texture details.

V. EXPERIMENT

In this section, we demonstrate a comprehensive evaluation of our proposed method. The qualitative and quantitative experiments are conducted on three benchmark datasets: the Synthetic NeRF dataset [1], the Tanks & Temples dataset [57], and the Mip-NeRF 360 dataset [51].

A. Dataset and Metrics

The rendering quality of our HRNVS is evaluated with respect to ground truth from the same pose using three metrics: Peak Signal-to-Noise Ratio (PSNR) and Structural Similarity Index Measure (SSIM) [58] and LPIPS (VGG) [59]. To evaluate our methods, we train and test our model on the following datasets:

Synthetic NeRF Dataset. [1] The synthetic NeRF dataset is a public dataset containing 8 scenes; each image has a resolution of 800×800 . Following the previous experimental settings, we used 100 images in each scene for training and

held out 200 images for testing. We downsample the training images by $2 \times$ (400×400) and $4 \times$ (200×200) using bicubic interpolation for downsampling and make them the input of $\times 2$ and $\times 4$ HRNVS tasks.

Tanks & Temples Dataset. [57] Tanks & Temples is a real-world dataset. The resolution is 1920×1080 , and we use a subset of 4 scenes. We use 1/8 of all views for testing and the rest for training. We downsample the training view by a factor of $2 \times$ (960×540) and $4 \times$ (480×270), using bicubic interpolation to serve as input to the $\times 2$ and $\times 4$ HRNVS tasks.

Mip-NeRF 360 Dataset. [51] Mip-NeRF 360 Dataset consists of 9 real-world scenes with 5 outdoors and 4 indoors, each containing a complex central object or area with a detailed background. Following the previous setup, We use 1/8 of all views for testing and the rest for training. We downsample the training view by a factor of $8 \times$, using bicubic interpolation to serve as input to the $\times 4, \times 8$ HRNVS tasks.

B. Implementation Details

We build our method upon the open-source 3DGS code. Following, we train 30K iterations across all scenes using the same hyperparameters and training schedule. For the 2D SR model, SWINIR [38] is selected as the backbone in SRGS. In addition, we set up our two loss functions, each loss takes the same form as 3DGS, and we use 0.4 for the control loss function hyperparameter λ . All our experiments are conducted on a single RTX 4090 GPU.

C. Performance Comparisons

To prove the effectiveness of SRGS, we conduct performance comparison with previous methods: NeRF variants, baseline (3DGS), Mip-splatting, and SR radiance field methods.

NeRF variants. Mip-NeRF 360 [51], and Zip-NeRF [50] are some classic methods of NeRF on unbounded complex scenes. We compared with them on the Mip-NeRF 360 dataset. We used LR training and HR rendering, and all results were achieved by running the official source code.

Baseline. 3DGS [2] as our baseline method has been successful on NVS tasks. For HRNVS, we train 3DGS with existing LR views and then perform HR rendering (3DGS). At the same time, we directly train 3DGS with HR multiple views as our theoretical upper limit (HR-3DGS). We conducted

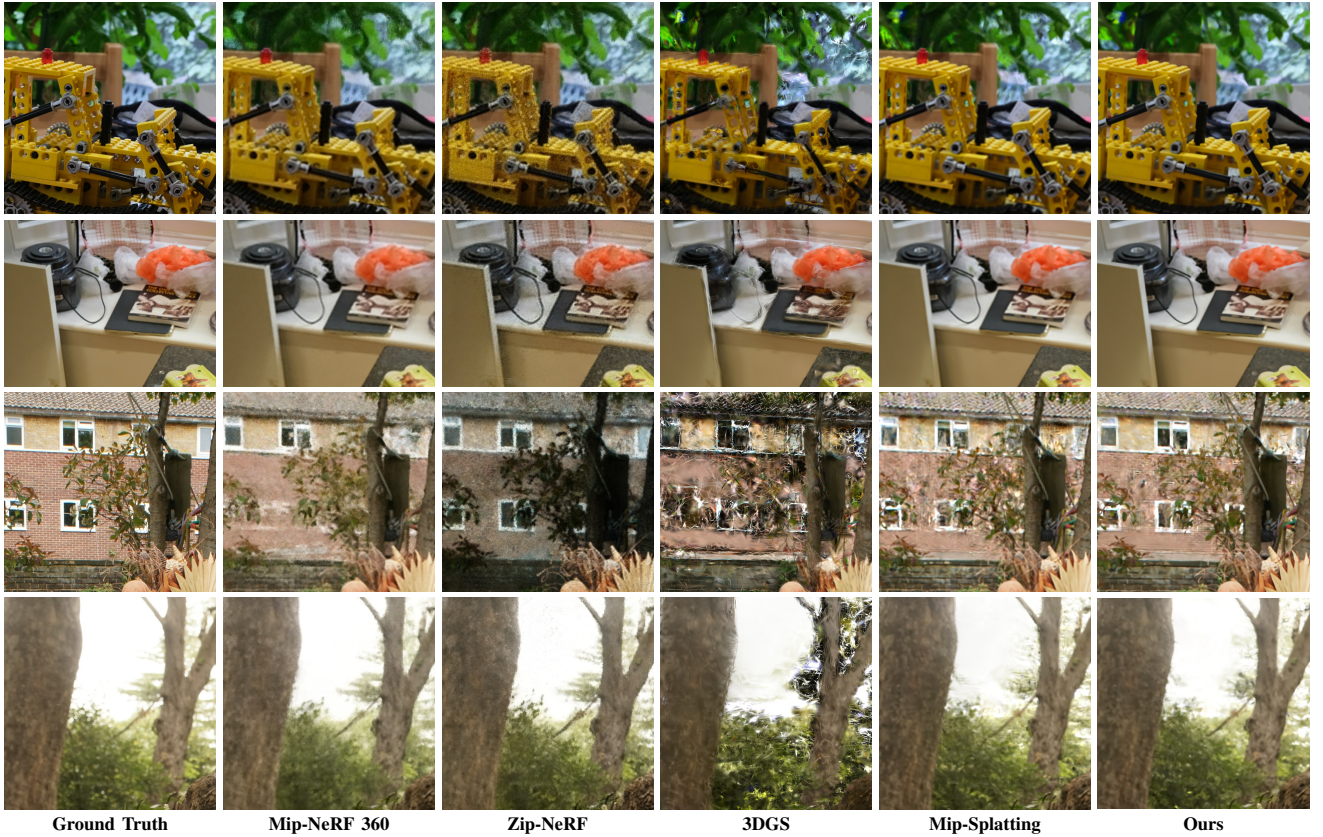


Fig. 5: Qualitative comparison of the HRNVS ($\times 8$) on the Mip-NeRF 360 dataset. Our method shows clearer details than Mip-NeRF 360, Zip-NeRF, 3DGS (baseline) and Mip-Splatting.

experiments directly on its source code to ensure fairness and the effectiveness of SRGS.

Mip-Splatting. Mip-Splatting [56] is a full-scale novel view synthesis method based on 3DGS. We ran its source code and obtained qualitative and quantitative results of HRNVS.

SR radiance field methods. NeRF-SR [48] and CROC [3] are the methods proposed for HRNVS with LR views. The CROC has reached the state-of-the-art in terms of rendering quality. For NeRF-SR, we directly run the source code to obtain qualitative and quantitative results. For CROC, which does not have open-source code, we conduct the experiment with the same settings and quote the data in the text for comparison.

D. Quantitative Evaluation

Table I demonstrates quantitative comparison results on the NeRF synthetic dataset and the Tanks & Temples dataset for $\times 2$ and $\times 4$ HRNVS tasks. The results highlight SRGS as a highly effective method, surpassing previous state-of-the-art approaches in the metrics of PSNR, SSIM, and LPIPS. Notably, SRGS outperforms the baseline method (3DGS) by more than 10 dB on the NeRF synthetic dataset, with an SR factor of 4. This is enough to prove the superiority of SRGS for HRNVS tasks. In addition, Mip-Splatting has a gain in rendering performance with two filters. However, there is still a certain gap in terms of texture information compared to SRGS. Table II shows the results of HRNVS with larger SR

factors such as $\times 4$ and $\times 8$ on the Mip-NeRF 360 dataset. The experimental findings indicate that SRGS continues to achieve the best outcomes, even in more challenging scenes with larger SR factors. This holds true even when comparing it to variant NeRF methods designed for unbounded complex scenes, such as Mip-NeRF 360 and Zip-NeRF.

E. Qualitative Evaluation

Fig. 4 presents qualitative results of the NeRF Synthetic dataset and the Tank & Temples dataset at an SR factor of 4. TensorRF and NeRF-SR get blurry results. The 3DGS as a baseline method suffers from needle-like and blurring artifacts due to the out-distribution rendering. Mip-Splatting improves artifacts with specific filters but still results in texture-less renderings. Through Gaussian densification and texture learning, SRGS well addresses these problems, achieving visual effects that are both artifact-free and textured. Notably, the gear of Lego and the shadow of Caterpillar demonstrate significant improvements. Fig. 5 showcases the qualitative result of the Mip-NeRF 360 dataset at an SR factor of 8. The high-quality visual results of SRGS can be seen in the outdoor scene of Garden and the indoor scene of Kitchen. In comparison, 3DGS exhibits strong artifacts, while Mip-Splatting lacks detailed texture.

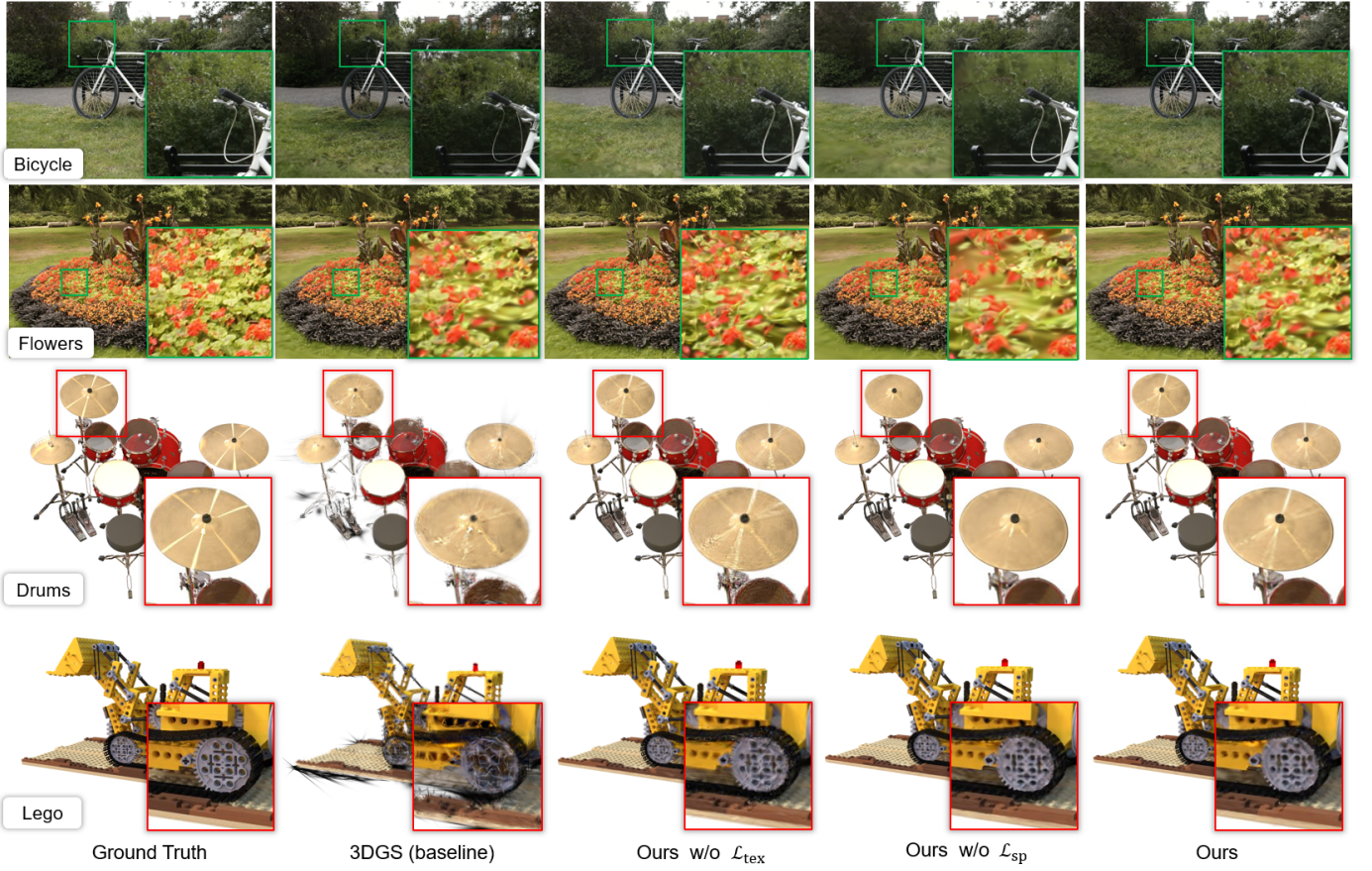


Fig. 6: Qualitative evaluation for ablation studies. The visualization results of the ablation experiments on \mathcal{L}_{sp} and \mathcal{L}_{tex} . \mathcal{L}_{tex} provides more textures for SRGS, but the spatial blur caused by texture inconsistency needs to be alleviated through \mathcal{L}_{sp} guidance.

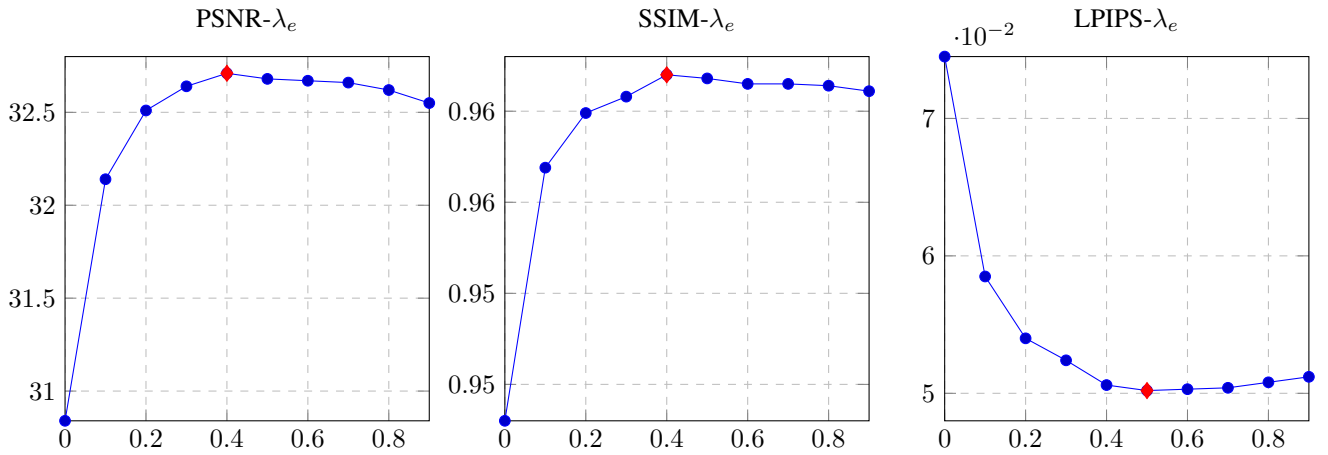
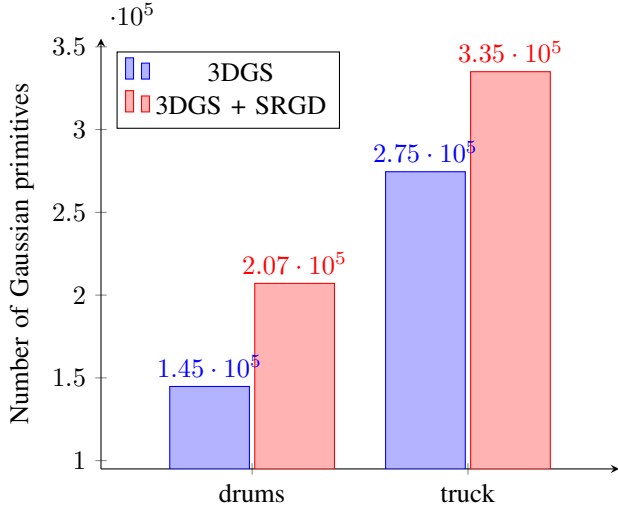


Fig. 7: The analysis of the weight-balancing parameter λ_e in total loss. When λ_e is 0.4, SRGS achieves the best performance

TABLE III: Ablation studies on Synthetic NeRF and MipNeRF 360 dataset for HRNVS ($\times 4$).

Method	Synthetic NeRF $\times 4$			MipNeRF 360 $\times 4$		
	PSNR \uparrow	SSIM \uparrow	LPIPS \downarrow	PSNR \uparrow	SSIM \uparrow	LPIPS \downarrow
3DGS (baseline)	20.31	0.852	0.121	20.71	0.619	0.394
Ours (w/o \mathcal{L}_{tex})	29.46	0.933	0.071	25.96	0.726	0.330
Ours (w/o \mathcal{L}_{sp})	30.38	0.945	0.059	26.66	0.762	0.301
Ours	30.83	0.948	0.056	26.88	0.767	0.286

Fig. 8: The statistical results on HRNVS ($\times 4$) regarding the quantity of primitives in the 3DGS and 3DGS + SRGD methods.

F. Ablation Studies

In Table III, we conduct ablation experiments on Super-Resolution Gaussian Densification (SRGD) and Texture-Guided Gaussian Learning (TGGL), respectively. It clearly demonstrates how SRGS gradually enhances the representation power of Gaussian primitives.

Effectiveness of SRGD. Referring to the second row of Table III, the proposed SRGD strategy demonstrates a significant improvement in PSNR, with a gain of 9 dB on the Synthetic NeRF dataset and 5 dB on the Mip-NeRF 360 dataset. Meanwhile, the annoying artifacts present in 3DGS renderings are mitigated, as depicted in Fig. 6. This

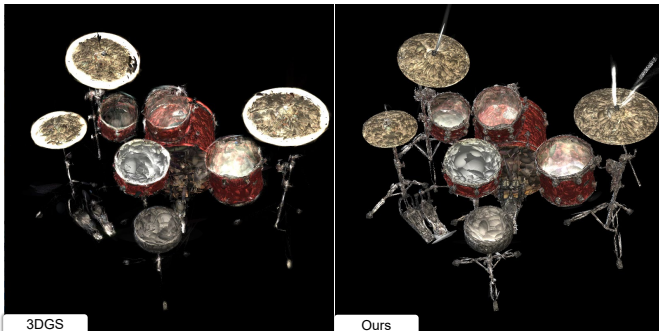


Fig. 9: The visualization results of Gaussian primitives. Our method significantly promotes Gaussian densification.

can be attributed to the improved representation power of densified Gaussian primitives. To prove that, we calculate the number of primitives in 3DGS models trained with and without SRGD. As shown in Fig. 8, the 3DGS with SRGD has a significant increase in the number of primitives compared to that without SRGD. The visualization result in Fig. 9 shows that more primitives are generated in the area with detailed textures. The above results demonstrate that SRGD effectively facilitates Gaussian densification, improving the render quality of HRNVS.

TABLE IV: Quantitative results for HRNVS ($\times 4$) on bonsai and bicycle scenes using different 2D SR models. The radiation fields trained directly on the SR results of 2D models are compared to those using our method.

Method	bonsai $\times 4$			bicycle $\times 4$		
	PSNR \uparrow	SSIM \uparrow	LPIPS \downarrow	PSNR \uparrow	SSIM \uparrow	LPIPS \downarrow
SwinIR [38]	31.27	0.922	0.206	24.15	0.659	0.364
Ours (SwinIR)	31.38	0.924	0.203	24.58	0.682	0.322
HAT [60]	31.51	0.934	0.193	24.25	0.662	0.357
Ours (HAT)	31.66	0.937	0.190	24.64	0.683	0.313
EDT [61]	31.64	0.933	0.197	24.56	0.664	0.346
Ours (EDT)	31.78	0.937	0.193	24.76	0.687	0.310

Effectiveness of TGGL. The proposed TGGL benefits from joint optimization with both external knowledge and sub-pixel constraints. The quantitative results in Table 6 illustrate the impact of excluding sub-pixel constraints or external knowledge, as well as the combined effect of both. It can be observed that the absence of either \mathcal{L}_{tex} or \mathcal{L}_{sp} leads to degradation performance, which highlights the indispensability of both components in achieving high rendering quality. When optimization is only based on sub-pixel constraints, the renderings exhibit texture deficiency. On the other hand, if optimization only relies on external knowledge, it can introduce considerable spatial ambiguity. However, the joint optimization with both of them faithfully captures textures and maintains spatial consistency. Therefore, the ablation experiments reveal two vital observations: (1) texture knowledge from the 2D SR model facilitates primitives to encode detailed textures in high resolution; and (2) the sub-pixel constraints from the LR views with realistic textures effectively mitigate the inconsistent textures generated by the 2D model. Moreover, we make an analysis for the weight-balancing parameter λ_e of both losses. Referring to Fig. 7, SRGS demonstrates the best performance in terms of PSNR and SSIM when $\lambda_e = 0.4$, whereas it performs best in LPIPS when $\lambda_e = 0.5$. When λ_e is set to 0.4 and 0.5, the performance on LPIPS is relatively close. Taking all aspects into consideration, $\lambda_e = 0.4$ is chosen in the training process.

Effectiveness of 2DSR model. In the proposed method, the prior knowledge an external 2D model is utilized to generate rich 3D texture information. Therefore, this section presents ablation experiments for different 2D SR models, further demonstrating the effectiveness of the method. In the experiments, we compare the rendering quality built on advancing 2D super-resolution models such as SwinIR [38], HAT [60], and EDT [61]. Notably, SwinIR is the model

employed in the main text. The HAT and EDT are the state-of-the-art models that outperform SwinIR. As shown in Table IV, our method exhibits robust enhancement when extended to different 2D models. This shows that our method can learn more faithful texture features from external priors. Meanwhile, the quality of textures learned on 3D models improves with the performance of 2D SR models.

VI. CONCLUSION

In conclusion, we present Super-Resolution 3D Gaussian Splatting (SRGS), a novel approach tailored for High-Resolution Novel View Synthesis (HRNVS) with exclusively low-resolution inputs. To the best of our knowledge, our method is the first attempt in this domain. Specifically, we first use the Super-Resolution Gaussian Densification strategy to densify the Gaussian primitives, enabling the representation of fine-grained high-resolution information. Furthermore, we introduce a Texture-Guided Gaussian Learning strategy that guides Gaussian primitives to learn faithful textures from external priors of the 2D super-resolution model. Experimental results on three public datasets show that SRGS effectively enhances the representation power of Gaussian primitives, approaching the rendering performance of 3DGS trained with high-resolution views. Notably, our SRGS is mainly limited by the 2D super-resolution model. In our future work, we will further explore the HRNVS methods without the 2D super-resolution model.

REFERENCES

- [1] B. Mildenhall, P. P. Srinivasan, M. Tancik, J. T. Barron, R. Ramamoorthi, and R. Ng, "Nerf: Representing scenes as neural radiance fields for view synthesis," in *European conference on computer vision*. Springer, 2020, pp. 405–421.
- [2] B. Kerbl, G. Kopanas, T. Leimkühler, and G. Drettakis, "3d gaussian splatting for real-time radiance field rendering," *ACM Transactions on Graphics*, vol. 42, no. 4, July 2023.
- [3] Y. Yoon and K.-J. Yoon, "Cross-guided optimization of radiance fields with multi-view image super-resolution for high-resolution novel view synthesis," in *IEEE/CVF Conference on Computer Vision and Pattern Recognition*, June 2023, pp. 12 428–12 438.
- [4] Z. Yan, W. F. Low, Y. Chen, and G. H. Lee, "Multi-scale 3d gaussian splatting for anti-aliased rendering," 2023.
- [5] M. Levoy and P. Hanrahan, "Light field rendering," in *Seminal Graphics Papers: Pushing the Boundaries, Volume 2*, 2023, pp. 441–452.
- [6] S. J. Gortler, R. Grzeszczuk, R. Szeliski, and M. F. Cohen, "The lumigraph," in *Seminal Graphics Papers: Pushing the Boundaries, Volume 2*, 2023, pp. 453–464.
- [7] R. A. Drebin, L. Carpenter, and P. Hanrahan, "Volume rendering," *ACM Siggraph Computer Graphics*, vol. 22, no. 4, pp. 65–74, 1988.
- [8] M. Levoy, "Efficient ray tracing of volume data," *ACM Transactions on Graphics (ToG)*, vol. 9, no. 3, pp. 245–261, 1990.
- [9] N. Max, "Optical models for direct volume rendering," *IEEE Transactions on Visualization and Computer Graphics*, vol. 1, no. 2, pp. 99–108, 1995.
- [10] N. Max and M. Chen, "Local and global illumination in the volume rendering integral," Lawrence Livermore National Lab.(LLNL), Livermore, CA (United States), Tech. Rep., 2005.
- [11] Z. Chen and H. Zhang, "Learning implicit fields for generative shape modeling," in *Proceedings of the IEEE/CVF conference on computer vision and pattern recognition*, 2019, pp. 5939–5948.
- [12] J. J. Park, P. Florence, J. Straub, R. Newcombe, and S. Lovegrove, "Deepsdf: Learning continuous signed distance functions for shape representation," in *Proceedings of the IEEE/CVF conference on computer vision and pattern recognition*, 2019, pp. 165–174.
- [13] L. Mescheder, M. Oechsle, M. Niemeyer, S. Nowozin, and A. Geiger, "Occupancy networks: Learning 3d reconstruction in function space," in *Proceedings of the IEEE/CVF conference on computer vision and pattern recognition*, 2019, pp. 4460–4470.
- [14] C. Sun, M. Sun, and H. Chen, "Direct voxel grid optimization: Super-fast convergence for radiance fields reconstruction," in *IEEE/CVF Conference on Computer Vision and Pattern Recognition*, 2022.
- [15] X. Zhu, J. Zhou, L. You, X. Yang, J. Chang, J. J. Zhang, and D. Zeng, "Dfie3d: 3d-aware disentangled face inversion and editing via facial-contrastive learning," *IEEE Transactions on Circuits and Systems for Video Technology*, pp. 1–1, 2024.
- [16] S. Fridovich-Keil, A. Yu, M. Tancik, Q. Chen, B. Recht, and A. Kanazawa, "Plenoxels: Radiance fields without neural networks," in *IEEE/CVF Conference on Computer Vision and Pattern Recognition*, 2022.
- [17] P. Hedman, P. P. Srinivasan, B. Mildenhall, J. T. Barron, and P. Debevec, "Baking neural radiance fields for real-time view synthesis," *IEEE/CVF International Conference on Computer Vision*, 2021.
- [18] L. Liu, J. Gu, K. Z. Lin, T.-S. Chua, and C. Theobalt, "Neural sparse voxel fields," in *Conference on Neural Information Processing Systems*, 2020.
- [19] T. Müller, A. Evans, C. Schied, and A. Keller, "Instant neural graphics primitives with a multiresolution hash encoding," *ACM Trans. Graph.*, vol. 41, no. 4, pp. 102:1–102:15, Jul. 2022.
- [20] X. Xie, R. Gherardi, Z. Pan, and S. Huang, "Hollownerf: Pruning hashgrid-based nerfs with trainable collision mitigation," in *Proceedings of the IEEE/CVF International Conference on Computer Vision*, 2023, pp. 3480–3490.
- [21] S. Girish, A. Shrivastava, and K. Gupta, "Shacira: Scalable hash-grid compression for implicit neural representations," in *Proceedings of the IEEE/CVF International Conference on Computer Vision*, 2023, pp. 17 513–17 524.
- [22] A. Chen, Z. Xu, A. Geiger, J. Yu, and H. Su, "Tensorf: Tensorial radiance fields," in *European Conference on Computer Vision*, 2022.
- [23] R. Shao, Z. Zheng, H. Tu, B. Liu, H. Zhang, and Y. Liu, "Tensor4d: Efficient neural 4d decomposition for high-fidelity dynamic reconstruction and rendering," in *Proceedings of the IEEE/CVF Conference on Computer Vision and Pattern Recognition*, 2023, pp. 16 632–16 642.
- [24] X. Feng, Y. He, Y. Wang, C. Wang, Z. Kuang, J. Ding, F. Qin, J. Yu, and J. Fan, "Zs-srt: An efficient zero-shot super-resolution training method for neural radiance fields," *arXiv preprint arXiv:2312.12122*, 2023.
- [25] H. Jin, I. Liu, P. Xu, X. Zhang, S. Han, S. Bi, X. Zhou, Z. Xu, and H. Su, "Tensorf: Tensorial inverse rendering," in *Proceedings of the IEEE/CVF Conference on Computer Vision and Pattern Recognition*, 2023, pp. 165–174.
- [26] S. Guo, Q. Wang, Y. Gao, R. Xie, L. Li, F. Zhu, and L. Song, "Depth-guided robust point cloud fusion nerf for sparse input views," *IEEE Transactions on Circuits and Systems for Video Technology*, pp. 1–1, 2024.
- [27] L. Yariv, P. Hedman, C. Reiser, D. Verbin, P. P. Srinivasan, R. Szeliski, J. T. Barron, and B. Mildenhall, "Bakedsf: Meshing neural sdf for real-time view synthesis," in *ACM SIGGRAPH 2023 Conference Proceedings*, 2023, pp. 1–9.
- [28] P. Hedman, P. P. Srinivasan, B. Mildenhall, J. T. Barron, and P. Debevec, "Baking neural radiance fields for real-time view synthesis," in *Proceedings of the IEEE/CVF International Conference on Computer Vision*, 2021, pp. 5875–5884.
- [29] A. Yu, R. Li, M. Tancik, H. Li, R. Ng, and A. Kanazawa, "Plenotrees for real-time rendering of neural radiance fields," in *Proceedings of the IEEE/CVF International Conference on Computer Vision*, 2021, pp. 5752–5761.
- [30] C. Reiser, S. Peng, Y. Liao, and A. Geiger, "Kilonerf: Speeding up neural radiance fields with thousands of tiny mlps," in *Proceedings of the IEEE/CVF international conference on computer vision*, 2021, pp. 14 335–14 345.
- [31] C. Reiser, R. Szeliski, D. Verbin, P. Srinivasan, B. Mildenhall, A. Geiger, J. Barron, and P. Hedman, "Merf: Memory-efficient radiance fields for real-time view synthesis in unbounded scenes," *ACM Transactions on Graphics (TOG)*, vol. 42, no. 4, pp. 1–12, 2023.
- [32] C. Dong, C. C. Loy, K. He, and X. Tang, "Image super-resolution using deep convolutional networks," 2014.
- [33] C. Dong, C. C. Loy, and X. Tang, "Accelerating the super-resolution convolutional neural network," in *Computer Vision – ECCV 2016*, B. Leibe, J. Matas, N. Sebe, and M. Welling, Eds. Cham: Springer International Publishing, 2016, pp. 391–407.

- [34] W. Shi, J. Caballero, F. Huszár, J. Totz, A. P. Aitken, R. Bishop, D. Rueckert, and Z. Wang, “Real-time single image and video super-resolution using an efficient sub-pixel convolutional neural network,” *CoRR*, vol. abs/1609.05158, 2016.
- [35] J. Kim, J. K. Lee, and K. M. Lee, “Deeply-recursive convolutional network for image super-resolution,” 2016.
- [36] B. Lim, S. Son, H. Kim, S. Nah, and K. M. Lee, “Enhanced deep residual networks for single image super-resolution,” in *IEEE/CVF Conference on Computer Vision and Pattern Recognition Workshops*, 2017.
- [37] Y. Zhang, K. Li, K. Li, L. Wang, B. Zhong, and Y. Fu, “Image super-resolution using very deep residual channel attention networks,” in *European Conference on Computer Vision*, 2018.
- [38] J. Liang, J. Cao, G. Sun, K. Zhang, L. Van Gool, and R. Timofte, “Swinir: Image restoration using swin transformer,” in *IEEE/CVF International Conference on Computer Vision Workshops*, 2021, pp. 1833–1844.
- [39] X. Wang, K. Yu, S. Wu, J. Gu, Y. Liu, C. Dong, Y. Qiao, and C. C. Loy, “EsrGAN: Enhanced super-resolution generative adversarial networks,” in *European Conference on Computer Vision Workshops*, September 2018.
- [40] C. Ledig, L. Theis, F. Huszár, J. Caballero, A. Cunningham, A. Acosta, A. Aitken, A. Tejani, J. Totz, Z. Wang *et al.*, “Photo-realistic single image super-resolution using a generative adversarial network,” in *Proceedings of the IEEE conference on computer vision and pattern recognition*, 2017, pp. 4681–4690.
- [41] L. Song, Y. Li, and N. Lu, “Profiles-gan: A gan based super-resolution method for generating high-resolution load profiles,” *IEEE Transactions on Smart Grid*, vol. 13, no. 4, pp. 3278–3289, 2022.
- [42] J. He, W. Shi, K. Chen, L. Fu, and C. Dong, “Gcfsr: a generative and controllable face super resolution method without facial and gan priors,” in *Proceedings of the IEEE/CVF conference on computer vision and pattern recognition*, 2022, pp. 1889–1898.
- [43] Z. Liu, Z. Li, X. Wu, Z. Liu, and W. Chen, “Dsrgan: Detail prior-assisted perceptual single image super-resolution via generative adversarial networks,” *IEEE Transactions on Circuits and Systems for Video Technology*, vol. 32, no. 11, pp. 7418–7431, 2022.
- [44] C. Saharia, J. Ho, W. Chan, T. Salimans, D. J. Fleet, and M. Norouzi, “Image super-resolution via iterative refinement,” *arXiv:2104.07636*, 2021.
- [45] Z. Yue, J. Wang, and C. C. Loy, “Resshift: Efficient diffusion model for image super-resolution by residual shifting,” *Advances in Neural Information Processing Systems*, vol. 36, 2024.
- [46] S. Gao, X. Liu, B. Zeng, S. Xu, Y. Li, X. Luo, J. Liu, X. Zhen, and B. Zhang, “Implicit diffusion models for continuous super-resolution,” in *Proceedings of the IEEE/CVF conference on computer vision and pattern recognition*, 2023, pp. 10 021–10 030.
- [47] G. Li, W. Xing, L. Zhao, Z. Lan, J. Sun, Z. Zhang, Q. Zhang, H. Lin, and Z. Lin, “Self-reference image super-resolution via pre-trained diffusion large model and window adjustable transformer,” in *Proceedings of the 31st ACM International Conference on Multimedia*, ser. MM ’23. New York, NY, USA: Association for Computing Machinery, 2023, p. 7981–7992.
- [48] C. Wang, X. Wu, Y. Guo, S. Zhang, Y. Tai, and S. Hu, “NeRF-SR: High quality neural radiance fields using supersampling,” in *ACM International Conference on Multimedia*, oct 2022.
- [49] J. T. Barron, B. Mildenhall, M. Tancik, P. Hedman, R. Martin-Brualla, and P. P. Srinivasan, “Mip-nerf: A multiscale representation for anti-aliasing neural radiance fields,” in *IEEE/CVF International Conference on Computer Vision*, 2021, pp. 5835–5844.
- [50] J. T. Barron, B. Mildenhall, D. Verbin, P. P. Srinivasan, and P. Hedman, “Zip-nerf: Anti-aliased grid-based neural radiance fields,” *IEEE/CVF International Conference on Computer Vision*, 2023.
- [51] —, “Mip-nerf 360: Unbounded anti-aliased neural radiance fields,” *IEEE/CVF Conference on Computer Vision and Pattern Recognition*, 2022.
- [52] Z. Zhang, W. Hu, Y. Lao, T. He, and H. Zhao, “Pixel-gs: Density control with pixel-aware gradient for 3d gaussian splatting,” 2024.
- [53] A. Haque, M. Tancik, A. A. Efros, A. Holynski, and A. Kanazawa, “Instruct-nerf2nerf: Editing 3d scenes with instructions,” in *Proceedings of the IEEE/CVF International Conference on Computer Vision*, 2023, pp. 19 740–19 750.
- [54] Y.-H. Huang, Y. He, Y.-J. Yuan, Y.-K. Lai, and L. Gao, “Stylizednerf: consistent 3d scene stylization as stylized nerf via 2d-3d mutual learning,” in *Proceedings of the IEEE/CVF Conference on Computer Vision and Pattern Recognition*, 2022, pp. 18 342–18 352.
- [55] Y. Han, T. Yu, X. Yu, Y. Wang, and Q. Dai, “Super-nerf: View-consistent detail generation for nerf super-resolution,” *arXiv preprint arXiv:2304.13518*, 2023.
- [56] Z. Yu, A. Chen, B. Huang, T. Sattler, and A. Geiger, “Mip-splatting: Alias-free 3d gaussian splatting,” *arXiv:2311.16493*, 2023.
- [57] A. Knapitsch, J. Park, Q.-Y. Zhou, and V. Koltun, “Tanks and temples: Benchmarking large-scale scene reconstruction,” *ACM Transactions on Graphics*, vol. 36, no. 4, 2017.
- [58] Z. Wang, E. Simoncelli, and A. Bovik, “Multiscale structural similarity for image quality assessment,” in *The Thirty-Seventh Asilomar Conference on Signals, Systems & Computers*, vol. 2, 2003, pp. 1398–1402 Vol.2.
- [59] R. Zhang, P. Isola, A. A. Efros, E. Shechtman, and O. Wang, “The unreasonable effectiveness of deep features as a perceptual metric,” in *IEEE/CVF Conference on Computer Vision and Pattern Recognition*, 2018, pp. 586–595.
- [60] X. Chen, X. Wang, W. Zhang, X. Kong, Y. Qiao, J. Zhou, and C. Dong, “Hat: Hybrid attention transformer for image restoration,” *arXiv preprint arXiv:2309.05239*, 2023.
- [61] W. Li, X. Lu, S. Qian, J. Lu, X. Zhang, and J. Jia, “On efficient transformer and image pre-training for low-level vision,” *arXiv preprint arXiv:2112.10175*, 2021.